4.0 MATERIAL AND METHODS

4.1 FIELD SETTING

Lake DePue is a moderately sized (*ca.* 524 acres) backwater lake of the Illinois River located in central, northern Illinois, about 20 kilometers west of LaSalle and 170 kilometers west of Chicago. Land use in the region is primarily agricultural. Lake DePue is connected to the Illinois River by a narrow channel at the west end of the lake. The lake is very shallow in the summer months, with a maximum depth of approximately 2 m as measured in July of 1998. Shallow parts of the lake, especially at the northwest and east end, consist of wide, marshy areas. The water during typical sampling periods is extremely turbid with a high concentration of suspended solids. Industrial chemical operations, including zinc smelting, sulfuric acid production, and di-ammonium phosphate fertilizer production, have led to substantial metal and nutrient contamination of the aquatic system. The zinc smelting operations took place in DePue from 1906 to 1971. In 1967, the capacity of the plant was 71,000 tons per year (Gibb and Cartwright, 1982).

The sediments in the lake are composed of lightly colored particles and are generally loose, fluffy, and unconsolidated. Sedimentation rates in the lake have been reported up to 3-4 cm per year (Cahill and Steele, 1986). Erosion of banks, bluffs, and the adjacent and upland soils all contribute to the sediment load of the Illinois River. Poorly sorted silt and clay alluvium dominate the surficial deposits along most of the river. In addition, bluff materials also include loess and tills that have a high clay mineral content (Willman, 1973). The fine-grained part of this sediment wash load is the principal source of sediment in backwater lakes (Lee, 1984).

4.2 FIELD SAMPLING

Initially, three major sampling sites were chosen along a gradient of contamination in the lake (see Figure 4.1).

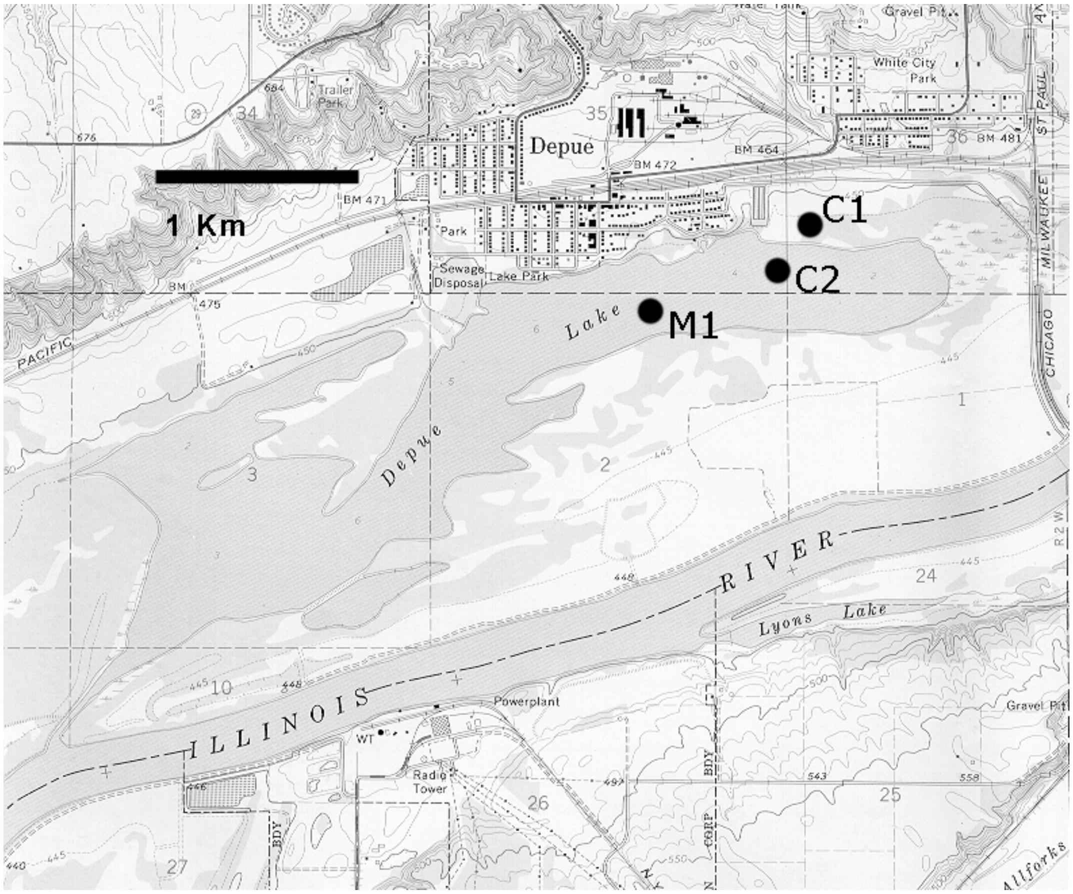

Figure 4.1: Location of sampling sites in Lake DePue, IL. Inset shows location of DePue, IL, approximately 170 km west of Chicago, IL.

The first site, C1, is located in a highly contaminated, shallow stream which drains into the lake. This is the point source from which most of the contamination appears to enter the lake. Zinc concentrations are approximately 300 µM in the stream and up to 30% by dry weight in the sediments. The stream flows in Lake DePue at site C2. Since the lake is a backwater lake, the stream and lake levels are highly variable depending on the season. Due to the variability of runoff, this collection site has a deltaic sedimentation pattern. Total zinc ranges from 2 to 10% by dry weight. The last sediment collection site, M1, is located away from the bulk of the zinc contamination, in the middle of the lake. Zinc concentrations in these sediments are close to background for the region (~100 ppm) except for the upper 1 cm of freshly sedimented material that contains up to 0.5% zinc. The sediment in this location is considerably more consolidated than at C1 and C2 and could not be penetrated by hand coring more than 15 cm.

4.2.1 Water Column Sampling

At each sediment sampling location, CTD-Oxy (Conductivity, Temperature, Depth, Oxygen) profiles in the water column were acquired using a Hydrolab MiniSonde probe, defining of the general physicochemical environment above the sediments. Conductivity was calibrated at the beginning of the field season, whereas depth, oxygen, and pH were calibrated on each sampling trip. Conductivity was calibrated by placing the electrode sensor in a standardized 0.005 M KCl solution, which gives a specific conductance of 0.718 mS/cm. The pH sensor was calibrated in standard NBS buffers at pH 4 and pH 7. Depth is calibrated simply by placing the probes at the air-water interface of the lake. Dissolved oxygen was calibrated by immersing the probe in air equilibrated water (100% saturation) and noting the barometric pressure. A barometer was carried into the field to record accurately the uncorrected barometric pressure.

Water samples were collected using clean sampling procedures from a 10-foot rubber boat (Zodiac Z-Force 10). All samples were placed in plastic bottles (Nalgene) that were thoroughly acid washed with dilute nitric acid. Samples from the water column were collected using a peristaltic pump equipped with cleaned Tygon® vinyl tubing. The end of the tubing was weighted and placed at the appropriate depth and sample collected into a 60 mL syringe. This prevents the exposure to oxygen before filtration for anoxic samples. Sample aliquots (both unfiltered and filtered water using a 0.2 µm cellulose acetate syringe filter) were placed into clean bottles. Samples for metals were preserved immediately by addition of SUPRAPUR™ trace metal grade concentrated HNO_3. The spread of the contaminant plume into the lake was examined with a global positioning system (GPS) study, where the position of each surface water sample was taken by a differential GPS measurement. Samples of the surface water were collected along a sampling grid extending from the creek outlet in to the lake.

4.2.2 Sediment Sampling

Sediments were collected using the piston coring method. This method places a core barrel with a piston at the sediment water interface. This method of coring has the advantage of keeping the core strata intact, unlike dredge sampling, and minimizing core compression. The piston is held in place while the core barrel is pushed into the sediment. The piston places the core under suction so that it can be easily removed from the sediment. As the core is raised, a second piston is placed at the bottom immediately after removal to prevent any leakage of the sample. Cores were typically 25 to 75 cm in length. Once brought back to shore, the core was subsampled. This was performed by slicing 1 cm increments of the core into clean containers or subcoring utilizing a 60 mL syringe with the tip cut off. Subcores were sealed with core cappers and placed into a customized airtight box that was installed with a rubber stopper in order to purge the contents with N_2 gas. Subcores that were saved for X-ray absorption analysis were placed into liquid N_2 and stored under cryogenic conditions (liquid N_2) in order to quench chemical and biological reactions and prevent exposure to oxygen. When short surface samples were desired (*i.e.* 10 cm or less), the sediments were sampled directly with the syringe subsamplers described above.

4.2.3 Porewater Sampling

The porewaters from Lake DePue sediments were collected using *in situ* porewater equilibrators, or "peepers" (Hesselein, 1976; Gaillard *et. al.*, 1986; Gaillard, 1993; Urban, 1997). Peepers consisted of a 63.5 x 10 cm solid, plexiglass body into which were milled 55 cells (0.5 x 7 cm) at a spacing of 1 cm. The cells were filled with Milli-Q water and a 0.2 μm filter (Tuffryn polysulfone membrane, Gelman, Inc.) was placed over the surface of the frame, which was secured by an outer plexiglass template 3 mm thick. Oxygen was removed from the water in the cells by immersing the peepers in a bath of Milli-Q water and purging with N_2 overnight. The peepers were then placed vertically into the sediments and the solutes in the porewater were allowed to diffuse into the cells. After equilibration, the concentration inside each cell corresponds to those at the respective depth in the sediment. Two to three weeks were allowed for equilibration to occur (Carignan, 1984).

The cells of the peeper were sampled immediately after removal from the sediments. Water from the cells was withdrawn using syringes equipped with pipette tips instead of needles. The sample was immediately injected onto containers containing the appropriate fixative agents. Samples for metals were acidified with SUPRAPUR™ trace metal grade HNO_3, samples for dissolved gas (CO_2 and CH_4) analysis placed into Vacutainer tubes in the presence of 1 M $HgCl_2$ to stop microbial reactions, and samples for sulfide analysis treated with 0.2 M zinc acetate. Samples for major anion analysis were placed into Falcon tubes kept at 5°C until analysis. Sampling of peepers was done as rapidly as possible to avoid the invasion of oxygen and evasion of other gaseous species. The sampling procedure generally took place within 15-30 minutes. Analysis of species was completed immediately after returning to the laboratory.

4.3 AQUATIC CHEMICAL METHODS

4.3.1 Colorimetric Methods

Several techniques utilizing colorimetric methods was used to measure dissolved Mn^{2+}, dissolved Fe^{2+}, and ΣH_2S species. These are described below. All methods measured the absorbance of the colored species spectrophotometrically against a reagent blank.

Dissolved Mn^{2+} was measured using the formaldoxime method (Goto *et. al.*, 1962; Morgan and Stumm, 1965; Chiswell and O'Halloran, 1991). The formaldoxime reagent was prepared by mixing 8.0 g of hydroxylamine hydrochloride with 4 mL of 30% w / w formaldehyde solution into a final volume of 100 mL of Milli-Q water. 2.5 mL of sample was mixed with 0.25 mL of formaldoxime reagent and 0.25 mL of ammonia (15% w / w) solution. The sample was allowed to stand for at least 2 minutes for the color to fully develop. The absorbance of the red-brown solution was measured at 450 nm against a reagent blank. The limit of reliable quantification for this method is approximately 250 nM for a 1 cm path length. However, a major interference of this technique is the reaction of formaldoxime with ferrous iron. This complex begins to have significant interference effects at concentrations of Fe^{2+} greater than 5 μM. Thus, ferrous iron was measured at the same time to account for the interference as described below with the ferrozine method. A calibration of Fe^{2+} was also performed with the formaldoxime reagent. In the cases where ferrous iron concentration was significant, the corresponding absorbance from the formaldoxime calibration was subtracted from the total absorbance of the sample. Thus the remaining absorbance was due to the manganese formaldoxime complex.

Ferrous iron was determined by the ferrozine method as described by Stookey (Stookey, 1970). This method was chosen since it is very selective, has few interferences, and because the colored complex has a high molar absorbtivity, providing low detection limits. The reagent was prepared using a 6 mM solution of the disodium salt of ferrozine. Approximately 0.25 mL of reagent is added to 2.5 mL of solution. Since the absorbance of the complex is maximized around pH 5, 0.25 mL of acetate buffer (pH = 4.75) was added. The resulting complex has a deep violet color whose absorbance was measured at 562 nm against a reagent blank. This method easily achieves quantitation limits of 100 nM with a 1 cm path length.

Sulfide species (Σ H_2S) was determined by the methylene blue method as given in the Standard Methods (Eaton *et. al.*, 1995). This method is based on the reaction of sulfide with N,N'-diamethyl-1,4-phenylenediamine to form 3-mercapto-N,N'-dimethyl-1,4-phenylenediamine. This product further reacts with another molecule of N,N'-diamethyl-1,4-phenylenediamine to form colorless leucomethylene blue. Leucomethylene blue is then oxidized by the addition of ferric iron. Samples collected in the field were preserved in the field by the addition of a 2 M zinc acetate solution in a 1:10 reagent to sample ratio. To insure complete precipitation of the zinc sulfide, the pH was raised to at least 9 with addition of 0.1 mL of 1 M NaOH per 5 mL sample aliquot. The reagent was prepared by dissolving 2.7 g N,N'-diamethyl-1,4-phenylenediamine into 50 mL concentrated H_2SO_4 and diluting to a final volume of 100 mL with water. The iron reagent was prepared by dissolving 6.6 g $FeCl_3$ $6H_2O$ into 40 mL of water. 1.5 mL of preserved sample was mixed with 0.5 mL of the reagent and 0.5 mL of the ferric iron solution. The solution was allowed to stand 3-5 minutes for complete color development. Ammonium phosphate was added at the end to eliminate any color interference from excess ferric iron. The absorbance of the blue colored solution was measure at 665 nm against a reagent blank. The sum of sulfidic species can be reliably measured down to concentrations of 1 μM using a 1 cm path length.

4.3.2 Heavy Metal Determinations

Total metal concentrations were determined through nitric acid extractions (Survey, 1989). About 50 to 100 mg of dry sediment was precisely weighed and added to approximately 10 g of concentrated HNO_3. The sediment mixtures were shaken and allowed to react overnight. The acid extract was then centrifuged to settle any small particles and an aliquot diluted with Milli-Q water to the appropriate dilution range and further acidified to 5% acid content. This extraction method, while accounting for many of the phases present in the sediment, will not extract all metals in the soil (*e.g.*, silicate bound metals are the major phase not represented). Extractable metals were determined by ion exchange with $MgCl_2$. 10 mL of 1 M $MgCl_2$ was added to 1 g of dry sediment and allowed to extract over night with intermittent shaking. The extracts were measured with inductively coupled plasma atomic emission spectroscopy (ICP-AES) (Thermo Jarrell Ash AtomScan 25), Zeeman correction graphite furnace atomic absorption spectroscopy (Z-GFAAS) (Varian SpectrAA-800), or flame atomic absorption spectroscopy (FAAS) (GBC 932AA) depending on the metal and the expected concentration. Table 4.1 gives a list of elements analyzed and the corresponding concentration ranges.

Table 4.1: Concentration ranges for common elements measured. The lower value is the lowest, quantifiable concentration.

Metal	Method	Concentration Range
Ca	ICP-AES	0.05 – 40 ppm
Mg	ICP-AES	0.05 – 40 ppm
Na	ICP-AES	0.1 – 40 ppm
K	ICP-AES	1 – 40 ppm
Zn	FAAS	0.02 – 5 ppm
Pb	Z-GFAAS	0.1 – 15 ppb
Cu	Z-GFAAS	0.5 – 50 ppb
Cd	Z-GFAAS	0.02 – 5 ppb
Ni	Z-GFAAS	0.5 – 20 ppb

4.3.3 Sequential Extraction

Sequential extractions were performed to determine the amount of metals that were associated with different chemical fractions of the sediment. The procedure aims to dissolve specific, targeted fractions in each step, thus releasing any associated metals. It is sequential in the fact that the extraction steps are performed one after the other on the same sediment sample. The main limitation of this technique is that the targeted phases are operationally defined (*e.g.*, they may dissolve more metals than they were designed for or metals from other phases) and that the dissolved metals may partition to other remaining reactive phases during the procedure. However, the extractions were performed to benchmark the speciation results obtained through X-ray absorption spectroscopy.

The procedure performed follows the guidelines and parameters published in previous work by Tessier, *et. al.* (Tessier *et. al.*, 1979). Approximately 2 grams of sediment initially extracted with 20 mL of 1 M $MgCl_2$ solution at pH 7 for one hour. This extraction targets ion exchangeable metals, or those metals that are loosely bound to particle surfaces. The suspension is centrifuged to settle the particles and the supernatant removed for later analysis. The remaining sediment is washed with Milli-Q water before the next extraction step. Second in the procedure is the extraction by 20 mL of 1 M sodium acetate at pH 5 for approximately four hours. This step in the extraction sequence targets carbonate phases. Again, the suspension is centrifuged, the supernatant saved for analysis, and the remaining sediment washed. The third step in the method is extraction with 25 mL of 0.1 M NH_2OH-HCl for 6 hours, which targets both iron and manganese oxides. Organic matter is targeted in the next extraction using a solution of 10 mL 0.02 M HNO_3 and 10 mL of H_2O_2. The solution is extracted at 85°C for 5 hours. The final step dissolves the remaining phases through a solution of concentrated aqua regia. The extractant is diluted to 5% acid before analysis. Any metals intimately associated with phases such as silicates will not be extracted since HF was not used in the residual extraction step. All analysis of zinc in each extractant was performed using GF-AAS as described in the previous section.

4.3.4 Capillary Electrophoresis

Major anions (Cl^-, SO_4^{2-}, NO_3^-, and acetate) were determined using capillary electrophoresis. A Waters Quanta 2000 Capillary Ion Analyzer equipped with a negative power supply was used for the analysis. Indirect UV detection was achieved at 254 nm. Normal fused silica capillaries, approximately 60-70 cm in length, 75 μM I.D. were obtained from PolyMicro Technologies (Phoenix, AZ). Samples were introduced to the capillary by using a 30 s hydrostatic injection from a height of 10 cm. The separation voltage used was 15 kV. The electrolyte used was composed of 5 mM chromate as the chromophore and 1 mM tetradecyl-trimethylammonium bromide (TTAB) as the osmotic flow modifier. Table 4.2 gives the detection limits for the anions measured and Figure 4.2 shows a typical electropherogram.

Table 4.2: Limits of detection for common anions by electrophoresis using the hydrostatic injection mode for 30 seconds. Limits of detection are the minimum quantifiable concentration of each anion.

Anion	**Limit of Detection**
Cl^-	10 μM
SO_4^{2-}	5 μM
NO_3^-	10 μM
Acet.	50 μM

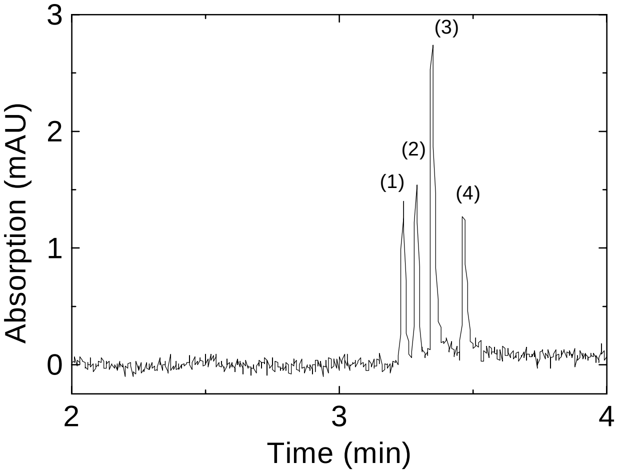

Figure 4.2: A typical electropherogram showing the separation of standard anions, all at a concentration of 100 μM: (1) Br^-, (2) Cl^-, (3) SO_4^{2-}, (4) NO_3^-.

4.3.5 Voltammetry

Voltammetry was used to determine the free or "electro-labile" concentrations of Zn, Cu, Pb, and Cd. This technique is an electroanalytical method that measures the current as a function of an applied potential waveform. A variable potential excitation signal is applied between a reference and working electrode that acts as the driving force for the electrochemical reaction. A reduction or oxidation reaction occurs at the surface of the working electrode whose electron transfer creates the current measured by the counter electrode. If electroactive species are present in solution, a current will be recorded when the potential becomes sufficient for the redox reaction to occur. This current is proportional to the analyte concentration in solution (Skoog and Leary, 1992). Anodic stripping voltammetry (ASV) can be used in order to achieve better detection limits for some metals. ASV effectively concentrates the metal by holding the potential for a set time (typically 60-360 s) at a potential more negative than the reduction potential of the analyte(s) of interest. Thus, the metal is reduced and is concentrated in the form of an amalgam with the mercury drop electrode. Note that this is only effective for those metals that can form an amalgam with mercury (*e.g.*, Zn, Cd, Pb, and Cu). After the preconcentration step, the potential waveform is applied as an anodic scan, and the current is measured versus the potential. When the potential becomes positive enough for the metal to be oxidized from the electrode surface into the solution, the oxidation results in a detectable current (Skoog and Leary, 1992).

Voltammetry was performed with a DLK-100 Electrochemical Analyzer (AIS) connected to a Metrohm 663 Voltammetric Analysis Stand. All measurements were performed in a three-electrode cell consisting of a hanging mercury drop (HMDE) working electrode, a Ag/AgCl (3 M NaCl) reference electrode, and Pt wire counter electrode. Both differential pulse anodic stripping voltammetry (DPASV) and square wave anodic stripping voltammetry (SWASV) were performed. Typical conditions for SWASV consisted of a scan of potential from –1.25 V to 0.00 V. The square wave parameters were: frequency 30: Hz; pulse height: 26 mV; scan rate: 100 mV/s; step width 33.3 ms. The deposition step was performed at a potential of –1.25 V for 120 seconds.

4.4 X-RAY ABSORPTION SPECTROSCOPY

4.4.1 Theory

A brief overview of the theory and processes involved in X-ray absorption spectroscopy will be given in this section. However, for a more comprehensive view, the reader should look to many of the comprehensive reviews that are available in the literature (Stern and Heald, 1983; Teo, 1986; Brown *et. al.*, 1988; Koningberger and Prins, 1988; Stern, 1988; Lytle, 1989). X-rays interact with matter in several ways. These interactions all include some type of excitation of, or scattering with, the matter involved. If an incident X-ray photon is of sufficient energy, the atom may absorb it. The absorption of the X-ray causes a photoelectron to be ejected from the atom in a process called photoionization, illustrated in Figure 4.3. This creates an excited state within the atom.

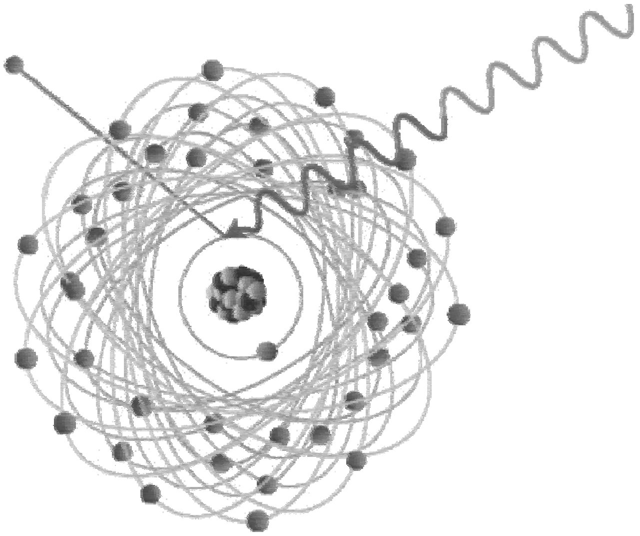

Figure 4.3: Illustration of photoinization initiated by the absorption of an X-ray photon. In this case, the illustration shows the ejection of a *1s* core electron. Figure taken from the APS Graphics Gallery, (www.aps.anl.gov / ald / grafgal2).

Several processes can occur after the absorption of the photon and subsequent ejection of a photoelectron in order to return the atom to its ground state. An outer shell electron may fill the shell vacancy created through photoionization, which creates a fluorescent X-ray photon. The fluorescent photon that is emitted is at a lower energy than the absorbed photon and is characteristic of the absorbing element. As atomic number increases, the fluorescent yield, or the probability that an absorption event will create a fluorescent photon, increases (Teo, 1986). For example, the K-shell (*1s*) fluorescent yields for O, Cl, Fe, Zn, Cd, and Pb are 0.0083, 0.097, 0.347 0.474, 0.843, and 0.967 respectively (Krause, 1979). The other major process following an X-ray absorption event is the Auger effect. In this case, the vacancy created by the photoelectron is filled by an electron dropping from a higher shell while the atom simultaneously ejects another electron. This additional electron is usually emitted from the same higher shell as the one that replaced the vacancy. This can be qualitatively thought of as an autoionization process, where the fluorescent photon created by the filling of the vacancy is energetic enough to ionize another electron from another shell of the same atom. However, the Auger effect is a one-step process where the atom readjusts to the initial vacancy rather than a two-step process. Finally, the photoionization of the atom can also create secondary electrons. These are created as the fluorescent X-ray or Auger electrons leave the atom and cause other high shell electrons to be ejected. This can be thought of as a cascade effect, and can be produced in abundant quantities.

X-rays also interact with matter through scattering processes. These are broken into two categories: coherent and incoherent. Coherent or Rayleigh scattering results from the interference between elastically scattered waves from individual atoms. In these cases, the photons are scattered by the atoms electrons that are bound tightly, and no ionization takes place. Since the scattering is elastic, there is no loss of energy, and thus the wavelength of the scattered radiation is the same. In crystals, this coherent scattering from a periodic lattice produces what is known as Bragg diffraction. Incoherent or Compton scattering takes place from interactions between the incident photons and loosely bound electrons. Part of the X-ray energy is transferred to the electron as the photon is scattered. Since energy is lost, the wavelength of the scattered X-rays will be shifted. For higher photon energies and heavier elements, the effects of scattering are several orders of magnitude less than that of absorption effects (Teo, 1986).

Given that absorption effects are dominant, we can describe the loss of intensity of an X-ray beam interacting with a sample by the absorption coefficient, μ. This loss is related to the original intensity of the beam, I, and the thickness of the sample, x, by $dI = -\mu I dx$. This can be integrated to give a familiar form of absorption of photons traveling through a substance,

$$\frac{I_T}{I_0} = e^{-\mu x}$$

where I_0 and I_T are the incident and transmitted X-ray intensities through the sample of thickness *x*. As the energy of the X-rays is increased, the absorption coefficient μ generally decreases gradually. This occurs until a critical energy is reached that where the coefficient increases abruptly by as much as an order of magnitude. For example, the μ for zinc changes from 260 cm^{-1} to 1897 cm^{-1} over 10 eV (McMaster *et. al.*, 1969). An illustration of X-ray absorption edges is given in Figure 4.4. This rapid change is due the X-ray photons reaching the energy at which an inner shell electron (*e.g.* the K shell (*1s*) or L shell (*2s* and *2p*)) can be ejected from the atom. The feature is called the absorption edge and is a unique characteristic of each element.

X-ray absorption spectroscopy (XAS) uses features within and around the absorption edge to examine various coordination properties of the element of interest. Two major regions are discussed within the context of spectroscopy. The first is called the X-ray

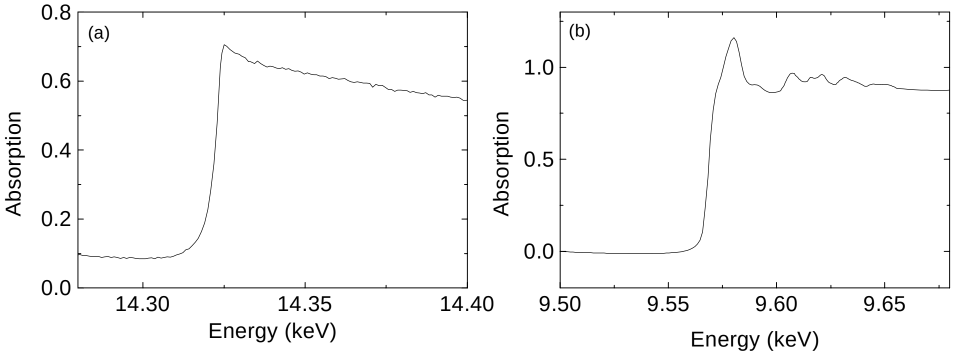

Figure 4.4: Sample X-ray absorption spectra for **(a)** a monoatomic gas (Kr) and **(b)** a Zn metal foil. Data from the F. Lytle database.
(http://ixs.iit.edu/database/data/Farrel_Lytle_data)

absorption near edge structure, or XANES for short. The XANES region generally consists of structure occurring in the pre-edge spectrum up to around 120 eV above the edge (Durham, 1988). Pre-edge features correspond to the excitation of core electrons to various bound states within the atom, i.e. transitions from the *1s* to the *nd*, (*n*+1)*s*, or (*n*+1)*p* orbitals for the K edge (Teo, 1986). The XANES features above the edge are generally due to a complex combination of effects including multiple scatterings, many body effects, band structures, etc. (Bianconi, 1988). These structures provide information on the electronic configuration, orbital energetics, and site symmetry of the atom examined. Additionally, the edge position also provides information on the charge of the absorbing atom, as a more positively charged atom will attract its core electrons more tightly, requiring slightly higher photon energies for photoionization (Williams and Lang, 1978). Unfortunately, the fundamental theory of XANES features is not as well understood as other aspects of XAS, and it is generally harder to calculate these features from first principles. Traditional quantitation by XANES involves using calibration curves based on either a pre-edge peak height or area vs. concentration in known standards (Szulczewski *et. al.*, 1997) or on edge energy shifts vs. the oxidation state of the standard (Bajt *et. al.*, 1994; Schulze *et. al.*, 1995).

The second region of interest in XAS is the Extended X-ray absorption fine structure (EXAFS). This region extends from the end of the XANES up to as much as 1200 eV above the edge. EXAFS is the final state interference effect between the ejected photoelectron from the absorption process and it scattering from neighboring atoms. In a qualitative quantum mechanical sense, the probability that an inner shell core electron will absorb a photon depends on the difference between the initial state and the final states of the electron. The initial state consists of the localized core level before the absorption event. The final state of the electron is that of the ejected photoelectron, which consists of photoelectron wave emanating from the atom. When, as in condensed matter, there are neighboring atoms, the outgoing photoelectron will be backscattered by these surrounding atoms. The intensity of the backscattered wave depends on numerous properties, including the neighboring atoms, the photoelectron wavelength, and the distance to the backscattering atoms. Thus the final state is a superposition of the outgoing wave and the sum of all backscattered waves. The constructive or destructive interference of these waves creates a modulation of the absorption coefficient above the edge. This is shown schematically in Figure 4.5. This modulation is the fine structure oscillations of interest in EXAFS. Since the fine structure is a function of the nearby short range neighboring atoms, compounds such as monoatomic gasses have no fine structure. This is seen in the absorption edge of Kr in Figure 4.4. In comparison, the Zn metal foil shown in Figure 4.4 shows significant fine structure in its absorption edge. Figure 4.6 qualitatively illustrates the differences between the XANES and EXAFS processes.

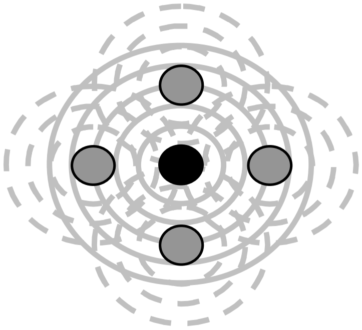

Figure 4.5: Schematic of the interference of outgoing and backscattered waves in the EXAFS phenomena. The process can be likened to throwing a rock into a lake that has 4 large stones in it. The wave created by the rock splashing into the water is scattered by its neighboring objects and thus the ripples observed at a distance are a combination of these interferences.

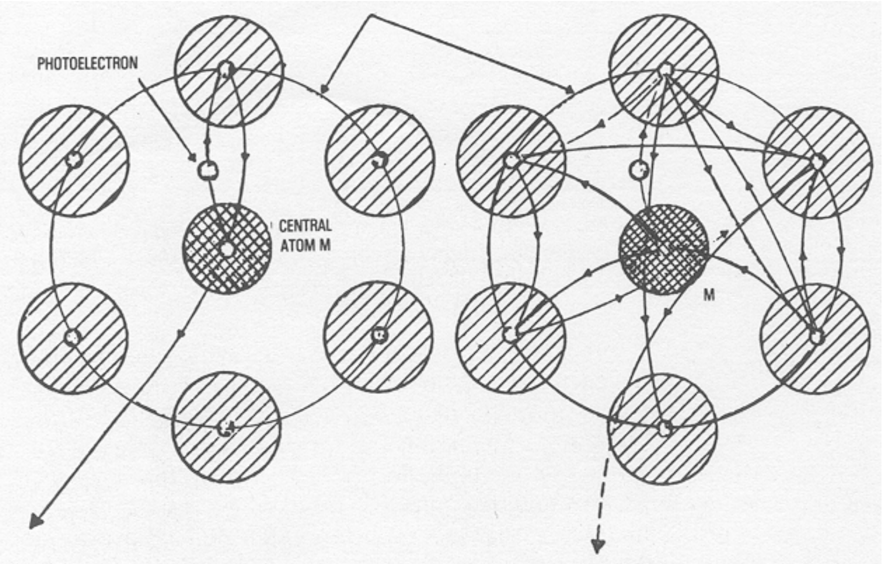

Figure 4.6: A cartoon illustration of the EXAFS (left) and XANES (right) processes. EXAFS generally consists of single scattering events, where the outgoing photoelectron is scattered by a single neighboring atom. The XANES phenomenon is created by a complex set of multiple interactions with the neighboring atoms [Bianconi, 1988 #49].

Many researchers have rigorously approached the theory of EXAFS. Kronig was one of the first investigators to propose that EXAFS was the result of a short-range order phenomenon rather than a large scale one (like diffraction). He proposed the current formulation of EXAFS as a final state wavefunction of the photoelectron caused by backscattering of local neighboring atoms (Kronig, 1932). A modern theoretical description of EXAFS based on *ab initio* parameters was developed in the early 1970's that has shown very good agreements with experimental data (Sayers *et. al.*, 1970). The development of this theory has allowed the extraction of atomic parameters, such as coordination number, neighboring atom types, bond lengths, and disorder parameters. The modulations of the EXAFS (χ) normalized by "background" absorption can be given as:

$$\chi(E) = \frac{\mu(E) - \mu_0(E)}{\mu_0(E)}$$

In order to relate the EXAFS to structural parameters, the absorption coefficient is changed from a function of energy (E) to a function of the photoelectron wavevector (k). This is done through an application of the de Broglie relation and Plank's constant. The theoretical form of EXAFS gives the χ as a sum of the contributions by each individual coordination shell. The EXAFS equation thus states that these oscillations in k-space are given by:

$$\chi(k) = \sum_j N_j S_i(k) A_j(k) e^{-2\sigma_j^2 k^2} e^{-2r_j/\lambda_j(k)} \frac{\sin(2kr_j + \phi_{ij}(k))}{kr_j^2}$$

where $A_j(k)$ is the backscattering amplitude from each of the N_j neighboring atoms of the j^{th} shell with a Debye-Waller factor of σ_j (accounting for thermal and static disorder) at a distance r_j from the central absorber, *i*. The total phase shift of the photoelectron from the backscattered shell is given by $\phi_{ij}(k)$. A reduction term given by the $e^{-2r/\lambda(k)}$ term is from inelastic losses in the scattering process from neighboring atoms and the medium, with λ_j being the electron mean free path. Finally, $S_j(k)$ is an amplitude reduction factor which accounts for many-body effects at the central atom (Teo, 1986).

It has been shown by Sayers, *et. al.*, 1971, that the isolated EXAFS can be Fourier transformed to determine the bond distances of the scattering atoms as a radial distance from the central absorbing atom. This analysis provided a key step in the development of modern XAS theory (Sayers *et. al.*, 1971). The transform actually only gives a pseudo-radial distribution function (RDF), as corrections for phase shifts must be applied to get the real distances. Figure 4.7 shows several of the steps in the data reduction process, from the raw spectrum, the normalized “unit step” spectra, the isolated EXAFS, and the Fourier transformed RDF. The implementation of these steps is explained in detail in Section 4.4.3 of the text.

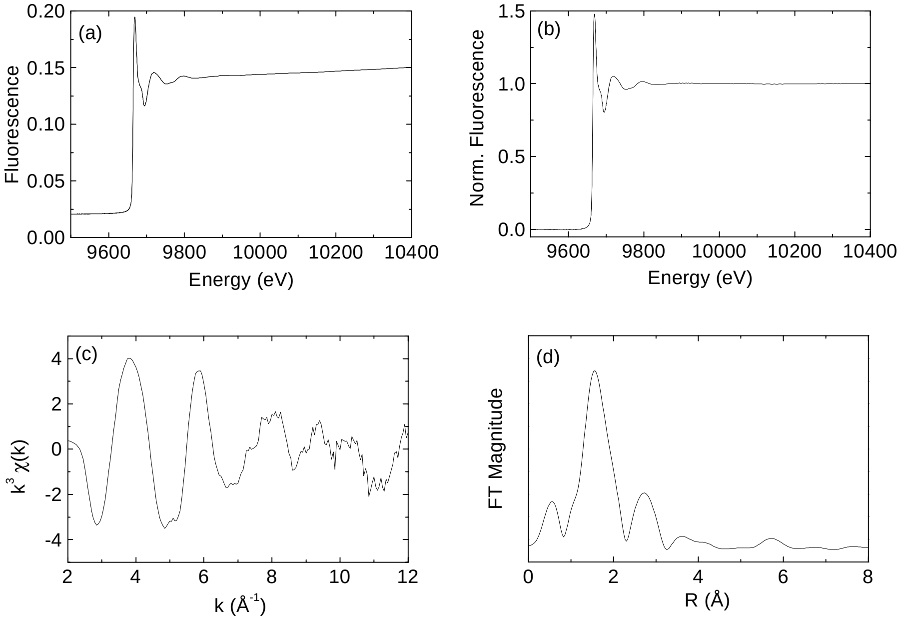

Figure 4.7: Plots showing the various steps in the data reduction steps in the analysis of EXAFS data: **(a)** raw data, **(b)** normalized spectra, **(c)** isolated and weighted EXAFS signal, **(d)** radial distribution function.

The experiment is carried out by measuring either the transmitted intensity or the fluorescence yield induced by the incident X-ray photons as a function of X-ray energy. Since the fine structure is a characteristic of the neighboring atoms around the central absorber, EXAFS spectroscopy provides a relatively non-invasive probe to determine the local structure of an element. The technique is applicable to a wide array of samples, including crystalline, polycrystalline, and amorphous solids, liquids, and gasses. In most typical applications of EXAFS, the sample examined is a pure phase compound. However, in environmental systems, the sample is rarely pure; rather it is a combination of several metal phases. Thus, traditional X-ray analysis using the EXAFS equation is not applicable. Since EXAFS is a spectroscopic technique, it has the property that the final absorption measured is a linear combination of the components in the system. Thus, one can use this property to analyze the make-up of the system. The application of a protocol to address this issue is discussed in Section 4.4.3 of the text.

The availability of synchrotrons for sources of X-ray has greatly improved the ability to perform EXAFS measurements on environmental and dilute samples. Advanced second and third generation synchrotron sources, such as the Advanced Photon Source at Argonne National Laboratory and SPEAR-3 at the Stanford Synchrotron Radiation Laboratory can provide greatly increased X-ray intensities over continuum X-ray tubes. These intensities have allowed measurement times for standard samples to drop from the order of a week (Lytle *et. al.*, 1975) down to minutes (Gaillard and Webb, ; Murphy *et. al.*, 1995; Solé *et. al.*, 1999) or even fractions of a second (Bornebusch *et. al.*, 1999).

Synchrotron radiation is created when a charged particle is accelerated. This phenomenon has been observed for many decades, and was initially an undesired feature in large high-energy particle accelerators. However, the unique properties of the light produced by synchrotrons were noticed, and specialized accelerators built to optimize those desired properties. For non-relativistic energies, the radiation emitted from the electron is in the classical dipole pattern, illustrated schematically in Figure 4.8a. The radiation emitted is distributed over a wide range of angles. Since the electron is in a circular orbit, the acceleration is perpendicular to the direction of motion, and as a result, the dipole pattern has a maximum in the direction of motion (Heald, 1988).

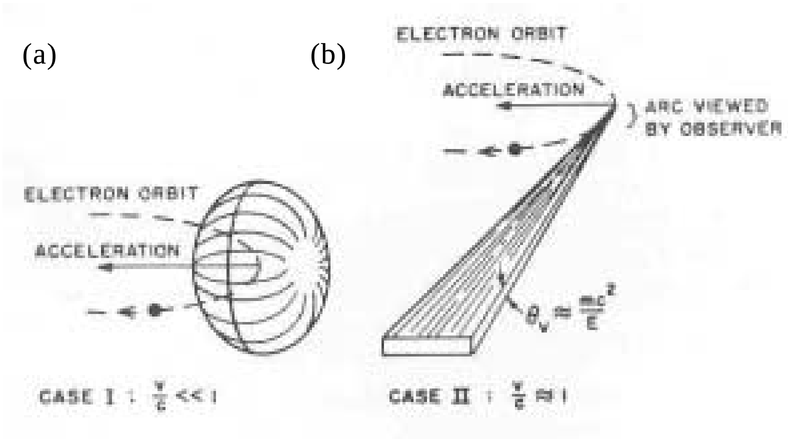

Figure 4.8: Radiation patterns emitted by charged particles (*i.e.*, electrons) for both the (a) non-relativistic classical dipole case, and the (b) relativistic case that exists in the synchrotron accelerator [Winick, 1980 #89].

However, as the electron speed reaches the speed of light, relativistic effects must be considered. The relativistic effect compresses the dipole pattern along the direction of motion resulting in a concentrated dipole tangential to the electron orbit (Margaritondo, 1988). This is illustrated in Figure 4.8b. The spectral distribution of bending magnet radiation is a function of the storage ring energy and the radius of curvature. The curvature can also be expressed as the bending magnet strength. The source characteristics are defined by the critical photon energy, given by

$$h\nu_c(\text{eV}) = (6.7\times10^2)B(\text{T})E^2(\text{GeV})$$

where B is the magnet strength in teslas and E is the storage ring energy in GeV. This is the value at which half of the irradiated power is emitted at photon energies above the critical energy and half below the critical value (Margaritondo, 1988). For the APS bending magnets, the critical energy is 19510 eV giving a peak flux of approximately 9.6

x 10^{13} photons/s/mrad^2/0.1% bw at 16.3 keV (Bizek, 1996). A diagram of the energy spectrum (in terms of brilliance) for the APS bending magnet and other synchrotron sources is given in Figure 4.9.

Photon flux can also be harnessed from insertion devices placed into the electron orbit of the storage ring. These are series of opposing polarity magnets placed into straight sections of the storage ring where there are no bending magnets. The series of alternating magnetic fields causes the electron beam to "wiggle" or "undulate" in the device around its normal trajectory. The net perturbation on the exit of the electron

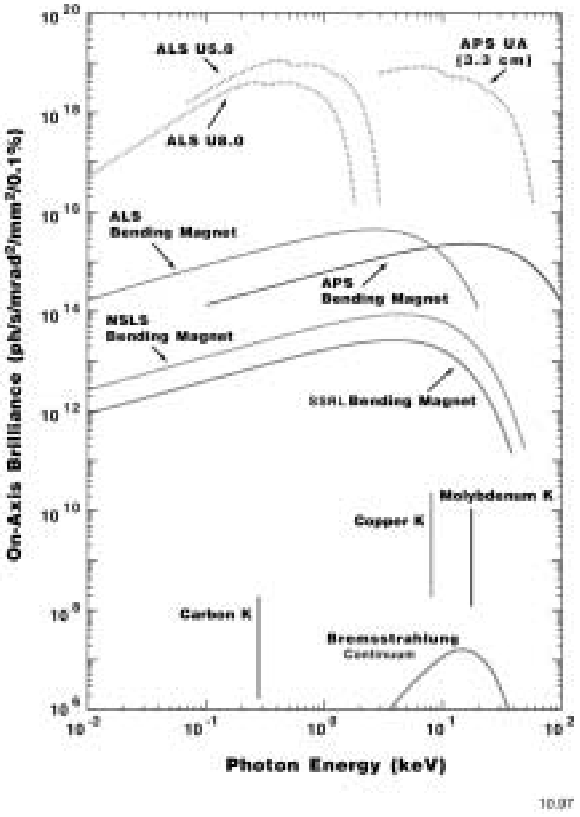

Figure 4.9: Photon brilliance as a function of X-ray energy for conventional and synchrotron radiation sources. Figure taken from the APS Graphics Gallery, (www.aps.anl.gov/ald/grafgal2).

from the device is minimized, so that there is little effect on the operation of the storage ring (Heald, 1988). A wiggler contains high magnetic fields and forces the electrons through extremely tortuous paths. Each oscillation creates synchrotron radiation, concentrated along the major axis of the insertion device. Wiggler radiation does not produce interference effects between the individual poles, so the spectrum produced is essentially the equivalent superposing a number of bending magnets that is roughly 2 times the number of periods in the wiggler array. The spectral distribution characteristics are also similar to that of the bending magnet source. The undulator insertion device has a larger number of periods in the array and weaker magnetic fields. As a result, interference effects create radiation that is highly concentrated (*i.e.*, very small bandwidth) around specific energies and its harmonics. This can be tuned by the user to the desired energy by altering the magnetic field strength in the undulator. In practice, this is done by changing the gap distances between the poles of the magnets in the array (Margaritondo, 1988). The bandwdith of the undulator can be increased by tapering the gap of the array. This causes the electron to go through a series of oscillations with varying periods, creating a more continuous spectrum (Lai *et. al.*, 1993). Examples of tapering the undulator are shown in Figure 4.10. The creation of a high intensity, continuous spectrum is highly advantageous for dilute and environmental XAS experiments.

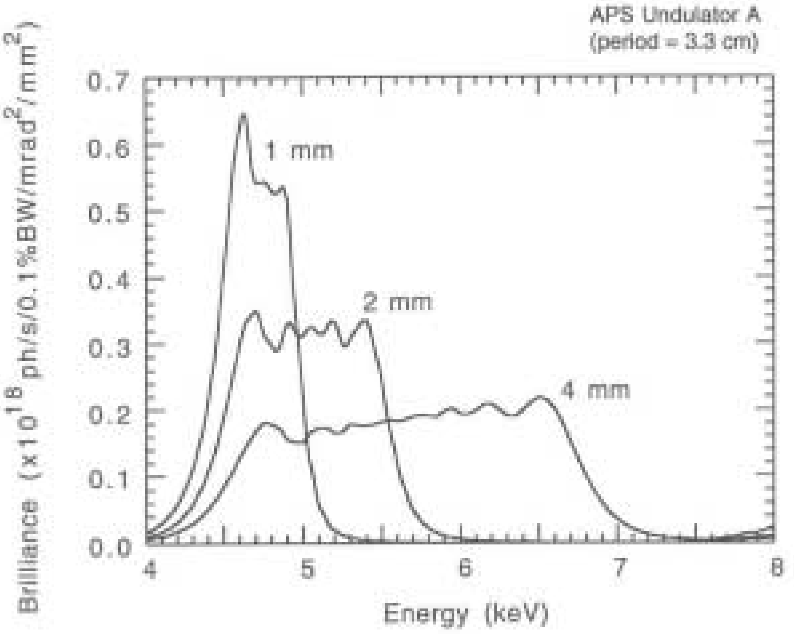

Figure 4.10: Source characteristics of the APS Undulator A as a function of the taper applied. This figure shows the spectrum of the first harmonic at an energy of approximately 4.25 keV [Lai, 1993 #88].

4.4.2 Experimental

X-ray absorption measurements were performed at the Advanced Photon Source, Argonne National Laboratory on the DND-CAT bending magnet and undulator insertion device beamlines. A detailed description of the CS-XAFS experimental setup can be found in Quintana (Quintana,) and Appendix A, which is summarized briefly in Figure 4.11.

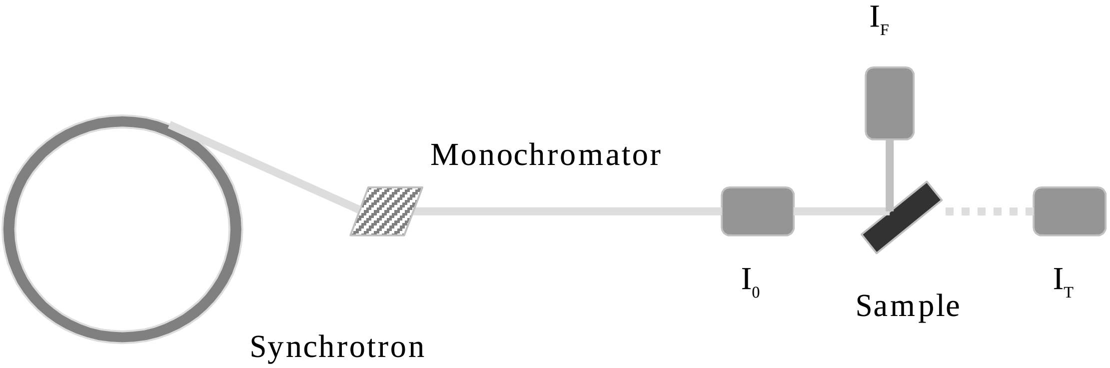

Figure 4.11: XAS experimental setup, not to scale. See text for description.

A Si(111) double crystal monochromator was used to vary the X-ray energy from 200 eV below to 1200 eV above the absorption K edge of either Zn (9659 eV) or Cd (26711 eV). The monochromator was detuned to approximately 75% of the maximum intensity to avoid harmonic interference. The incident intensity, I_0, and transmitted intensity, I_T, were measured by appropriately positioned ionization chambers. The fluorescence signal, I_F, was measured with a Stern-Heald detector (Lytle cell) equipped with a Z-1 Cu filter. The Z-1 filter is used to reduce the noise created by elastically scattered X-rays. For example, when examining a zinc (Z=30) sample, one would use a copper (Z=29) filter. Copper has an absorption edge at 8979 eV so it will absorb X-rays greater than its edge while allowing the zinc K_α fluorescence at 8630 eV to pass. Thus scattered X-rays from the beam at the energies of the scan (for zinc from 9669 eV to 10600 eV) will be attenuated greater than that of the fluorescence from the sample.

The output of the Lytle detector and ionization chambers were used as input to Stanford Research System SRS 570 Current Amplifiers. The output of these amplifiers was continuously oversampled at a 12.5 kHz rate with a sixteen-bit analog to digital converter (ADC). Data were collected while the monochromator was continuously slewed between the beginning and ending energies. Nine successive scans were recorded for each sample at a rate of 120 seconds per scan.

4.4.3 Data Analysis

Data were analyzed using a series of in-house perl scripts and Scilab (INRIA, Le Chesnay, France) codes linked with a Tcl/Tk graphical user interface. The details of the use of these scripts and codes are given in Appendix B. The codes were developed to specifically address the issue of analyzing CS-XAS data and propagating the error associated with the collection and processing of the data.

As mentioned, a key part of the data analysis is the propagation of error throughout the process. The CS-XAS technique allows the calculation of the experimental error based on the statistics of oversampling. As the monochromator is slewed, the A-D converter oversamples the detectors at a rate of 12.5 kHz. This creates huge data files, which can easily add up to 5 or 10 MB per scan. To reduce the volume of data, the data are divided in to bins that span a specified eV or k-space interval. The data reported as the value in that bin is the average of all of the measurements taken in the bin. In the XANES pre-edge region, this amounts to approximately 740 samples, whereas in the far-EXAFS region, there are about 6800 samples per bin. In each bin, the average and error associated with the bin is calculated. Each bin contains *N* oversamples of the same measurement, given that a bin covers a relatively small interval. The average value for the measurement is simply the sum of all the measurements, divided by the number of measurements, *N*. Each of these individual samples has an uncertainty associated with it. This error in each of these measurements can be expressed as the standard deviation of the samples in the entire bin. If we assume that the samples in the bin all have the same uncertainty, using the standard propagation of errors theorem, the error of the average value of the bin is

$$\sigma^2 = \left(\frac{1}{N}\right)^2 N\sigma_i^2$$
$$\sigma = {\sigma_i}\big/{\sqrt{N}}$$

where σ_i is the error of the individual measurements. This reflects the actual experimental error that arises from counting statistics and electronic noise in the system. For most of the spectral range, the measurements are normally distributed within a bin. The exception to this is in the pre-edge region, where it appears to be more of a Lorentzian distribution. Also, in the edge, where the absorption coefficient changes rapidly, 60 Hz noise within the monochromator leads the observation of a dual-Gaussian distribution within each bin. However, this only occurs for a few points in the overall spectrum. Measures to eliminate this noise need to be taken in order to correct this problem. Although this one region has slightly skewed distributions, a standard normal distribution was used when propagating the errors through the rest of the calculations in the EXAFS data reduction. To improve the signal to noise ratio, the multiple scans of the sample were averaged together and the errors were carried through with the standard propagation of errors theorem.

Since the normalization and extraction of the EXAFS signal processes are complicated procedures, the errors for these properties were calculated using a pseudo-Monte Carlo method. For the normalization process, a value of 2 sigma of the error was added to the original data signal. The error-induced signal was then fitted in the pre-edge region by a linear fit and in the EXAFS region by a quadratic. This process was repeated 1000 times, and the coefficients for each fit stored. The average value of the coefficients was then used to remove the background signal. The error of the signal was determined by the standard deviation of each of the fitting coefficients. A similar process was used in the isolation of the EXAFS $\chi(k)$. Again, the error of 2 sigma was added to the original signal. AUTOBK (Newville *et. al.*, 1993) was then used independently to remove the background signal, isolate $\chi(k)$ and store the array of data values. This was repeated 1000 times, and the final $\chi(k)$ determined by the average of the 1000 calculations. The error of these values was determined by the standard deviation of the replicates. In each of these steps, it was determined that $n = 1000$ repetitions was sufficient for the pseudo-Monte Carlo method by applying a range of repetitions from $n = 10$ to $n = 100{,}000$. The answers obtained did not significantly change after $n = 1000$ in all steps of the data processing.

4.4.4 Spectral Decomposition

The particular problem at hand with the analysis of EXAFS from environmentally relevant samples is how to determine the composition of the sample. Each phase that involves the element of choice will contribute to the total EXAFS signal. These phases may include minerals, amorphous precipitates, organic complexes, or aqueous complexes to mention a few. The goal is to examine the EXAFS spectrum to determine the proportions of each of these possible phases. This can be accomplished through spectral decomposition, which is used across many fields, from remote sensing (Maselli, 1998) to mathematics (Lange, 1992).

Spectral deconvolution can be applied in many different ways. In essence, one assumes that a signal is composed of a linear combination of signals from well-defined end member components. The method attempts to deconvolute the relative signal that each of the end members contributes to the measured signal at each point in the spectrum. Several different methods were applied in the decomposition of the sediment EXAFS over the development of the routine. The general approach to the solution is to find a vector, $\mathbf{f}$, which solves the equality $\mathbf{D} = \mathbf{f}\,\mathbf{M}$. In this scenario, $\mathbf{f}$ is the composition vector, $\mathbf{M}$ is a matrix of standard end members, and $\mathbf{D}$ is the vector containing the data spectrum. In the simplest sense, the solution can be obtained by a right matrix multiplication of the inverse of the matrix **M**,

$$\mathbf{D}\,\mathbf{M}^{-1} = \mathbf{f}\,\mathbf{M}\,\mathbf{M}^{-1}$$

$$\mathbf{D}\,\mathbf{M}^{-1} = \mathbf{f}$$

Since the number of components in the basis set of standard end members is less than the number of points in the data spectrum, the answer found in this manner is given in the least squares sense. Another approach is to use a singular value decomposition (SVD) routine. SVD is particularly useful if the solution becomes singular, which can occur if two components of the matrix **M** fit the data equally well or equally poor (Press *et. al.*, 1988). However, both of these solution algorithms have no constraints on what the vector **f** may be. In particular, it may readily provide components that have a negative contribution to the spectrum. This result, of course, is nonsense, as a component in a sediment sample may not have a negative concentration. This can be avoided by applying a non-negative least squares regression routine to deconvolute the spectrum. However, this method typically just removes components that have a negative contribution from the matrix **M** in the process of solving the problem. Although this may work in some cases, it is subject to fall prey to local minima when simply ignoring entire components in the standard matrix.

In particular, using k^3-weighted EXAFS data, the well-posed problem that is to be solved is to find a solution to:

$$k^3\chi_{\text{sample}}(k) = \sum_i f_i k^3 \chi_{\text{standard}-\text{i}}(k)$$

with the two constraints that:

$$\sum_i f_i = 1 \qquad\qquad f_i \geq 0$$

These constraints imply that the concentration of each component must be non-negative (there can be no negative mass), and that the sum of all the components must be one (there can be no missing mass). The approached used herein to tackle the constrained minimization is quadratic linear programming (QLP). In matrix form, QLP minimizes:

$$\left\|\mathbf{Mf}-\mathbf{D}\right\|^2$$

The minimization is subject to:

(a) the sum to one constraint

$$\mathbf{1}^{\mathrm{T}}\mathbf{f}=\begin{bmatrix}1 & 1 & \ldots & 1\end{bmatrix}\mathbf{f}=1$$

(b) the positivity constraint

$$f_i \geq 0, \text{for all } i$$

Thus, the linear quadratic programming problem minimizes:

$$\frac{1}{2}\mathbf{f}^{\mathrm{T}}\mathbf{Hf}-\mathbf{c}^{\mathrm{T}}\mathbf{f}$$

where $\mathbf{H} = \mathbf{M}^{\mathrm{T}}\mathbf{M}$, and $\mathbf{c} = \mathbf{M}^{\mathrm{T}}\mathbf{D}$ subject to the same constraints given above. The composition of mixtures was determined by this QLP approach to fit of the EXAFS signals of samples to standards. Again, the error in the fitting procedure was determined by using a pseudo-Monte Carlo method (n = 1000) where the 2 sigma error was applied to the sample and standards. The final value was determined by averaging the results of the 1000 replicates and the error of the fit by the standard deviation of the result.

The main caveat in this technique is aquiring a complete and *unique* database of appropriate standard compounds for the **M** matrix. The composition of the sample can only be as accurate as the standards chosen to represent the forms of the element in the sample. In addition, the matrix must consist of standards that all are unique in their spectral characteristics and independent of each other, *i.e.*, a standard cannot be a linear combination of any other standards. If this is not true, the basis set of standards will not be orthogonal, and the solution provided will not be accurate. For this study, these properties were checked using principal component analysis (PCA). PCA showed that the standard matrix, **M**, was independent, as the variance in the data could only be explained by including all of the components. Choosing fewer than all of the components in the matrix resulted in an unsatisfactory degree of variance to be explained, *i.e.*, over 5 percent. PCA can also be used to determine the minimum number of components needed to explain the variance present in a set of sediment samples. This gives another check on the QLP algorithm. If the basis set is truly orthogonal, the number of components determined by QLP should agree with the number of components needed to explain the bulk of the variance.

Standards for analysis of zinc were chosen after a careful geochemical analysis of Lake DePue sediments (Webb *et. al.*, 2000). By performing a survey of the elemental associations present in the sediment particles, one can compile a database that contains the most likely phases expected in the sediments. Mineral standards included sphalerite: ZnS; zincite: ZnO; amorphous zinc hydroxide: $Zn(OH)_2$; smithsonite: $ZnCO_3$; zinc phosphate: $(Zn_3(PO_4)_2)$; and zinc carbonate hydroxide: $(Zn_3CO_3(OH)_4)$. In addition to these mineral phases of zinc, aqueous zinc, zinc bound to manganese oxide, zinc bound to iron oxides (goethite, lepidocrocite, and hematite), zinc acetate, zinc X, and a zinc-cysteine precipitate were also used as standards. Cadmium EXAFS was also performed for examining the coordination environment in microorganisms. Cadmium standards included: CdS, CdO, CdPO4, CdCO3, Cd(OH)2, Cd-acetate, Cd-X, and a Cd-cysteine precipitate. Aqueous samples of Cd included: aqueous Cd, Cd-citrate, Cd-salicylate, Cd-oxalate, and Cd-glutamate. The complexes were prepared by mixing 10 mM cadmium with a 500-fold excess of the ligand and the pH adjusted to 7. All EXAFS were k^3-weighted in the fitting procedure to better emphasize the EXAFS at large k. The fitting procedure was calibrated through measuring a known set of mixed standards of sphalerite, zincite, zinc carbonate hydroxide, and zinc phosphate. The FEFF8 *ab initio* calculation package (Leon *et. al.*, 1991; Rehr *et. al.*, 1992) was used to check the integrity of the standards.

The method was calibrated by measuring the CS-XAS spectra of binary, ternary, and quaternary mixes of standard compounds in known proportions. These spectra were then analyzed using the spectral decomposition protocol to determine the amount of each of the standards in the sample. The deconvolution was performed for both the XANES and EXAFS regions. Most of the error in this calibration is likely to occur from the inhomogeneity of the powders in the samples and differences in particle size distributions between the different components. The best way to account for this in the future is to make sure that standard analysis is performed with the X-ray source illuminating the entirety of the mixed sample, *i.e.* all of the weighed reference compound mixture is placed in the illumination of the beam. Calibration curves for several of the components are displayed for the XANES in Figure 4.12 (a-c) and the EXAFS in Figure 4.12 (d-f). These figures show the mixed composition of each sample on the x-axis and the result of the decomposition on the y-axis. Good agreement between the composition and the deconvolution can be seen as the slopes of the calibrations are all close to unity.

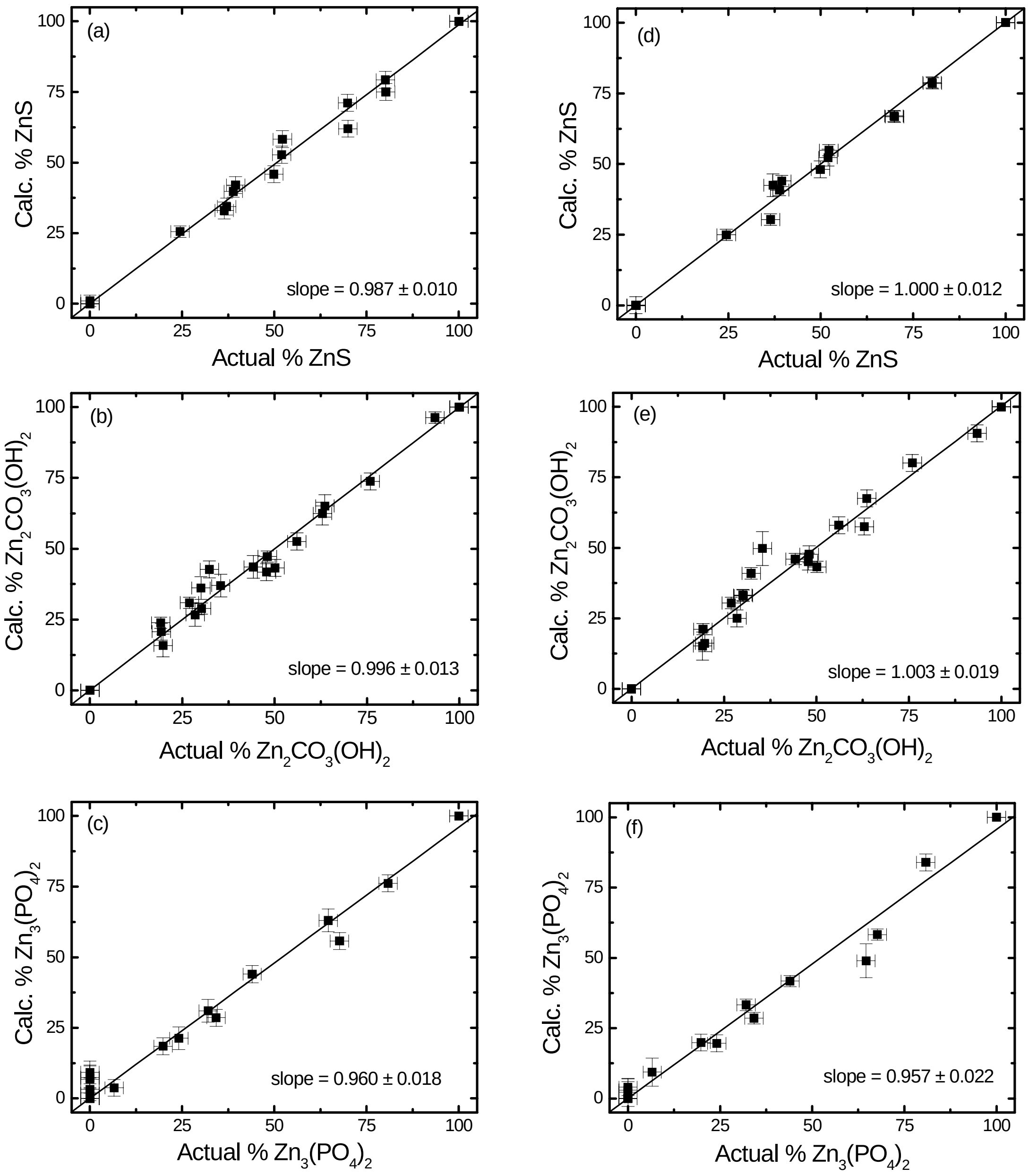

Figure 4.10: Calibration results of XANES **(a-c)** and EXAFS **(d-f)** spectral deconvolution method.

4.5 ELECTRON MICOSCOPY

4.5.1 SEM Analysis

Scanning electron microscopy (SEM) observations were performed to visualize particles and microbes from the water column and sediment of the lake. Samples were deposited on a 0.2 μM Nucleopore filter by filtration through a low flow vacuum water aspirator. All samples were diluted appropriately in the filtration step to avoid excessive coverage of the filter. This was done in order to minimize particle coagulation and aggregation artifacts on the filter. The filter was then placed onto a SEM stub using carbon tape. Samples were analyzed in low-vacuum mode on a Hitachi S-4500 cold-field emission SEM and variable pressure mode on a Hitachi S-3500N variable pressure SEM. Filters that were visualized in the low-vacuum mode were coated with gold to provide a conductive sink for the electrons. Samples in variable pressure mode were examined at a pressure of 3-10 torr. The accelerating voltage was 15 to 20 keV in all cases. X-ray energy dispersive spectroscopy (EDS) was performed to get the elemental composition of selected samples.

4.5.2 TEM Preparation Technique

Particles were stabilized and prepared for the production of ultrathin sections for transmission electron microscopy (TEM) using procedures that minimized dehydration artifacts (Leppard *et. al.*, 1996). A melamine resin (Nanoplast® FB101) was used as both a fixative and a hydrophilic embedding resin. This allows the preservation of extracellular structures and other colloids in their original hydrated form. The resin is prepared freshly by mixing 0.2 g of B52 catalyst (p-toluolsulfonic acid) to 10 g of hexamethylol-melamine-methyl ether (monomer MME7002). Aqueous samples were size fractionated through a sequential centrifugation process. Large particles in the raw surface water samples were removed by allowing the sample to gravitationally settle for 2.5 h. The supernatant was fractionated through centrifugation at 90g for 1 h. At each step in the sequential fractionation, the particles collected at the bottom of the tube were saved for EM analysis. Approximately 200 μL of Nanoplast® resin was added to a small smear of sediment or 50 μL of fractionated particles placed on a Teflon plate. The resin-sample mixtures were placed into an oven set a 40°C for 2 d in the presence of desiccant and, thereafter, without a desiccant at 60°C for another 2 d. This procedure ensures optimal properties for ultrathin sectioning (Frösch and Westphal, 1989) with a resolution limit of approximately 1 nm. After the Nanoplast resin was cured, the sample was removed from the Teflon plate and sliced into small strips, approximately 1-2 mm thick. These slices were then placed (vertical orientation) into a BEEM capsule (type 00 large with conical tip), which was then backfilled with Spurr's epoxy resin (Spurr, 1969). The capsule with its Spurr resin was placed into a 70°C oven for 8 h.

After polymerization was completed, all samples were sectioned identically. Ultrathin sections for morphological and EDS analysis (75-100 nm) were obtained by sectioning with a diamond knife mounted in a RMC Ultramicrotome MT-7. These sections were then mounted on formvar-covered copper grids. The grids were carbon-coated for stabilization in the EDS analysis. Although the Nanoplast® leaves the native spatial relations of the sample intact, it is often difficult in morphological studies to visualize structures rich in organic carbon. Applying an "electron-opaque" stain to the section on grids provides differential contrast leading to more readily visible organic structures; we applied a counterstain of 1% aqueous uranyl acetate for 3 hr (Leppard *et. al.*, 1996).

Ultrathin sections of embedded samples, mounted on formvar-coated, copper, electron microscope grids, were examined with a JEOL 1200 EXII TEMSCAN scanning-transmission electron microscope (STEM) operating at 80 keV. The characterization of particles by morphology was done with the TEM component of the STEM, which in turn allowed one to visually select specific particles or parts of particles for spectroscopy. Identification of detectable elements in mineral colloids was accomplished using energy dispersive spectrometry (EDS) microanalysis techniques. EDS was performed using the STEM equipped with a Princeton Gamma Tech Si(Li) X-ray detector in conjunction with a PGT IMIX multichannel analyzer. Analyses of element composition $Z > 10$ were made over counting periods (approximately 2 min.) appropriate to collecting sufficient counts while minimizing sample decomposition. ZAF standardless analysis (Heinrich, 1981; Reed, 1993; Reid *et. al.*, 1998) was carried out on each of the EDS spectra using the NIST Desk Top Spectrum Analyzer and X-ray Database program (Fiore *et. al.*, 1980).